*Journal of Marine Research, 50,* 421–440, 1992

# Models of abyssal flow in basins separated by a mid-ocean ridge

by Scott A. Condie[1,2] and Mitsuhiro Kawase[1]

ABSTRACT

Numerical and laboratory models have been used to study source-driven flows in a system consisting of two basins (with sloping sidewalls) separated by a mid-ocean ridge. Numerical spin-up occurs via topographically modified Kelvin waves which propagate away from the source region around the outer perimeter of the model ocean. Energy is then carried along the ridge by topographic waves and westward by planetary waves. The resulting flow eventually concentrates in strong cyclonic circulation patterns, defined by regions of closed geostrophic contours in the lower latitude portion of each basin. When the deep water source is located at the latitude of closed geostrophic contours, there is no significant flow outside the closed contours. However, when it is located further toward polar regions, strong flow is evident up to the source latitude. There is a close correspondence with the laboratory model when similarity conditions are satisfied. One notable difference was a higher level of wave and eddy activity in the laboratory, particularly near the border between closed and blocked contour regions.

## 1. Introduction

Deep ocean flows form an important link in the earths biogeochemical cycles. They modify climate and are now recognized as a useful indicator of climate change (Boyle and Keigwin, 1987; Labeyrie *et al.,* 1987). This in particular has led to renewed interest in their dynamics. A severe lack of detailed abyssal observations has limited the development of new theories; however there is some evidence that this is improving. One example which formed part of the motivation for the present study, is the Deep Basin Experiment (DBE) scheduled for 1992 in the Brazil Basin.

Models of abyssal flow have utilized three related, but quite distinct types of forcing. The first is inclusion of topography in wind driven circulation models (de Szoeke, 1985; Cessi and Pedlosky, 1986). One limitation of this approach is its sensitivity to the idealized form of the stratification, which tends to shield the deep flow from wind forcing in ways which are not well understood. Recent results from a stratified North Atlantic model (Huang, 1990) also suggest that the wind driven gyre may not penetrate beyond a depth of 2 km. The second type of forcing relates to what is traditionally referred to as flow over topography problems in which a specified

1. School of Oceanography WB-10, University of Washington, Seattle, Washington, 98195, U.S.A.
2. Present address: Research School of Earth Sciences, The Australian National University, GPO Box 4, Canberra, ACT 2601, Australia.

(usually uniform) flow interacts with isolated topographic features. Many of these types of studies have been motivated either by atmospheric phenomena (Smith, 1979; Blumen and Gross, 1987; Boyer and Chen, 1987) or by oceanic flows past isolated seamounts of a quasi-geostrophic horizontal scale (McCartney, 1975; Johnson, 1983; Thompson, 1990). Effects of planetary scale topography on the ocean circulation have been considered only recently (Rhines, 1989; Hogg, 1989). It should be remembered, however, that topography usually dominates over the influence of the planetary vorticity gradient ($\beta$ effect) for length scales typical of coherent mean flows in the ocean.

The $\beta$-effect becomes more important in a third type of forcing which forms the basis of the present study. This mechanism might be referred to as a "filling-box process." Because deep water formation results from convection at a few high latitude locations, there tends to be mean upwelling and corresponding vortex stretching over most of the abyssal ocean. On a flat bottom this results in the classic cyclonic Stommel-Arons circulation closed by deep western boundary currents (Stommel and Arons, 1960). Welander (1969) showed that when topography creates closed geostrophic contours (isolines of $f/H$ where $f$ is the Coriolis parameter and $H$ is the fluid depth) in the upwelling environment, western boundary currents are not required. This has recently been extended with the aid of numerical techniques by Straub and Rhines (1990) and Kawase and Straub (1991) for the case of an isolated seamount. Hautala and Riser (1989) revisited the mid-ocean ridge problem without closed geostrophic contours but included the more complex effects of surface wind forcing and geothermal heating.

The dominant topographic features in the ocean are the mid-ocean ridges which divide the ocean into a network of large-scale basins. A configuration which captures the essential features of this is a single ridge dividing two basins. Previous studies of adjoining basins have only considered the case in which the side walls (excluding the ridge itself) are vertical so that most geostrophic contours are blocked. The circulation can then only be closed by strong internal dissipative jets as proposed by Cessi and Pedlosky (1986). From a dynamical perspective, oceanic geostrophic contours might be considered blocked when contour gradients are sufficiently strong that flow is forced into narrow jets. However, even with this definition, a large fraction of deep ocean contours should be regarded as closed. The present models produced closed contour regions by including sloping side walls.

In Section 2 the model equations will be described and scaled velocities derived for closed and blocked contour regions. Details of both the numerical and laboratory models are given in Section 3, followed by their respective results in Sections 4 and 5. Section 6 concludes the study.

## 2. Equations of motion and scaling

In both the numerical and laboratory simulations, abyssal water is represented by a shallow homogeneous layer overlain by a deep motionless upper layer. This system

obeys the shallow water equations. In spherical coordinates, the zonal momentum equation is

$$\frac{\partial u}{\partial t} - (f + \zeta)v = -\frac{1}{R_e \cos\theta}\frac{\partial}{\partial \phi}\left(g'h + \frac{u^2 + v^2}{2}\right) - \frac{u}{\tau}, \tag{1}$$

while the meridional equation is

$$\frac{\partial v}{\partial t} + (f + \zeta)u = -\frac{1}{R_e}\frac{\partial}{\partial \theta}\left(g'h + \frac{u^2 + v^2}{2}\right) - \frac{v}{\tau}. \tag{2}$$

Here $(u, v)$ are the zonal ($\phi$) and meridional ($\theta$) velocity components; $f = f_0 + \Delta f$ is the planetary vorticity where $f_0 = 2\Omega \sin\theta_0$ is the value at the midlatitude $\theta_0$;

$$\zeta = \frac{1}{R_e \cos\theta}\left(\frac{\partial v}{\partial \phi} - \frac{\partial}{\partial \theta}(u \cos\theta)\right) \tag{3}$$

is the relative vorticity; $h$ is the interface perturbation; $g'$ is the reduced gravity and $R_e$ is the radius of the earth. Dissipation takes the form of Rayleigh bottom friction with a spin-down time-scale $\tau$. The shallow water continuity equation can be written

$$\frac{\partial h}{\partial t} + \frac{1}{R_e \cos\theta}\left(\frac{\partial}{\partial \phi}(u[h + H - D]) + \frac{\partial}{\partial \theta}(v[h + H - D]\cos\theta)\right) = W, \tag{4}$$

where $H$ is the average unperturbed depth of the layer measured from the abyssal seafloor. $D(\theta, \phi)$ is the height distribution of the topography, which here consists of a square basin with exponentially sloping side-walls, bisected meridionally by a Gaussian ridge (Fig. 1). The source term $W(\theta, \phi)$ is the volume flux per unit area directed into the abyssal layer. The total inflow rate is

$$Q = \int\int WR_e^2 \cos\theta \, d\theta \, d\phi. \tag{5}$$

The values of all dimensional quantities used in both the numerical and laboratory models are listed in Table 1.

The following nondimensional variables are now introduced,

$$x' = \frac{\phi R_e \cos\theta}{L_0}, \quad y' = \frac{\theta R_e}{L_0}, \quad h' = \frac{g'h}{Uf_0L_0}, \quad D' = \frac{D}{D_0},$$
$$u' = \frac{u}{U}, \quad v' = \frac{v}{U}, \quad W' = \frac{WL^2}{Q}, \quad t' = \frac{Ut}{L_0}, \quad \Delta f' = \frac{\Delta f}{\beta L_0}, \tag{6}$$

with appropriate velocity scales $U$ to be determined below. Substituting (6) into (1)–(4) and dropping the primes yields the non-dimensional momentum and continu-

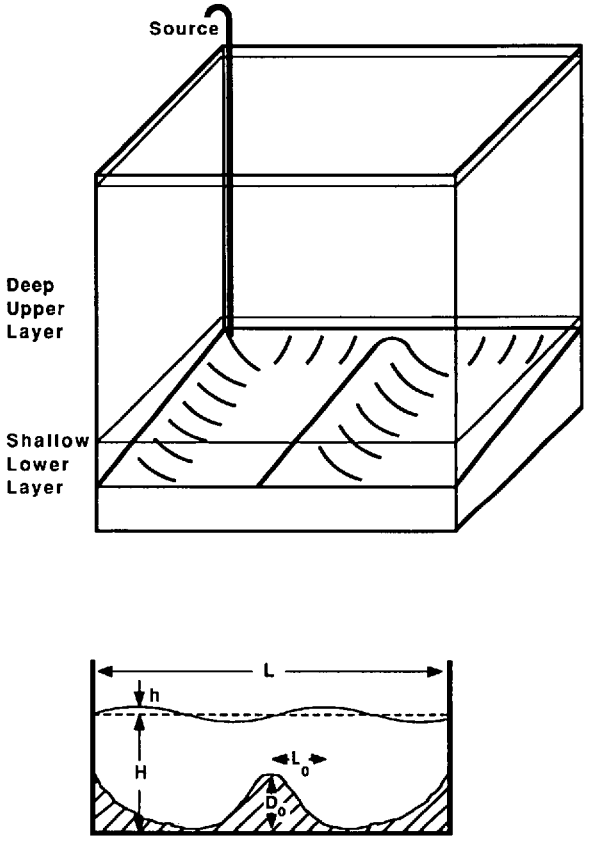


Figure 1. Schematic illustration of the flow configuration. This consisted of a light upper layer, beneath which a source of dense fluid flowed into a dense layer overlying topography. The lower illustration shows a zonal cross-section of the mid-ocean ridge topography.

ity equations,

$$R\frac{\partial u}{\partial t} - (1 + B\Delta f + R\zeta)v = -\frac{\partial}{\partial x}\left(h + R\frac{(u^2 + v^2)}{2}\right) - E^{1/2}u, \tag{7}$$

$$R\frac{\partial v}{\partial t} + (1 + B\Delta f + R\zeta)u = -\frac{\partial}{\partial y}\left(h + R\frac{(u^2 + v^2)}{2}\right) - E^{1/2}v, \tag{8}$$

$$R\frac{\partial h}{\partial t} + \frac{\partial}{\partial x}(u\eta) + \frac{\partial}{\partial y}(v\eta) = \mathrm{SE}^{1/2}\left(\frac{Q\tau}{HL^2}\right)W, \tag{9}$$

where the nondimensional parameters are defined in Table 2. The non-dimensional local layer depth is given by

$$\eta = Rh + S - \gamma SD, \tag{10}$$

Table 1. Values of dimensional variables from both the numerical simulations and the laboratory experiments. Underlined values are those chosen specifically to achieve similarity with the laboratory flows and correspond to the numerical solutions in Figure 9. When the laboratory spin-down time was calculated from (27), a depth representative of the southern half of the basin ($H$ = 9 cm) was used since most of the flow was concentrated in this region.

| Quantity | Symbol | Numerical | Laboratory |
|---|---|---|---|
| basin size | $L$ | 4000 km | 70 cm |
| active layer depth | $H$ | 2000 m | 7.0 cm |
| maximum topographic height | $D_0$ | 1000 m | 3.5 cm |
| topographic $e$-folding scale | $L_0$ | 400 km | 7.0 cm |
| mid-latitude planetary vorticity | $f_0$ | $8.0 \times 10^{-5}$ s$^{-1}$ | 2.0 s$^{-1}$ |
| planetary vorticity gradient | $\beta$ | $2.0 \times 10^{-11}$ m$^{-1}$s$^{-1}$ | $2.9 \times 10^{-2}$ cm$^{-1}$s$^{-1}$ |
| reduced gravity | $g'$ | 0.05, <u>0.15</u> ms$^{-2}$ | 8.4 cms$^{-2}$ |
| source strength | $Q$ | 4, <u>27</u> Sv | 0.75 cm$^3$s$^{-1}$ |
| spin-down time | $\tau$ | <u>26</u>, <u>100</u> days | 14 rotations |

which is of order $S$ for $R < S$. Until $U$ is explicitly determined, the Rossby number is taken to be $R = U/f_0L_0$. Free slip conditions are applied at the boundaries $x = 0,\lambda$ and $y = 0, \lambda$, where $\lambda$ is also defined in Table 2.

Kawase and Straub (1991) recently derived the velocity within a circular closed contour on an $f$-plane and a generalized version of this theory is used here to

Table 2. Definitions and values of non-dimensional variables for both the numerical simulations and the laboratory experiments. The underlined values again correspond to Figure 9.

| Quantity | Symbol | Definition | Numerical | Laboratory |
|---|---|---|---|---|
| height ratio | $\gamma$ | $\frac{D_0}{H}$ | 0.50 | — |
| length ratio | $\lambda$ | $\frac{L_0}{L}$ | 0.10 | — |
| aspect ratio | $\delta$ | $\frac{D_0}{L_0}$ | $2.5 \times 10^{-3}$ | 0.50 |
| Burger number | $S$ | $\frac{g'H}{f_0^2L_0^2}$ | 0.10, <u>0.30</u> | 0.30 |
| Beta number | $B$ | $\frac{\beta L_0}{f_0}$ | 0.10 | — |
| Ekman number | $E$ | $\frac{1}{\tau^2 f_0^2}$ | $2.1 \times 10^{-6}$, <u>$3.2 \times 10^{-5}$</u> | $3.2 \times 10^{-5}$ |
| Rossby numbers | $R_c$ | $\frac{Q\tau}{HL^2}$ | $1.1 \times 10^{-3}$, <u>$1.9 \times 10^{-3}$</u> | $1.9 \times 10^{-3}$ |
| | $R_b$ | $\frac{Q}{\beta HLL_0^2}$ | $1.6 \times 10^{-4}$, <u>$1.1 \times 10^{-3}$</u> | $1.1 \times 10^{-3}$ |

determine the appropriate velocity scale $U$. Neglecting terms of order $R$, $E$ and smaller, (7) and (8) approximate to,

$$u = u_g - \frac{E^{1/2}}{(1 + B\Delta f)} v_g, \tag{11}$$

$$v = v_g + \frac{E^{1/2}}{(1 + B\Delta f)} u_g, \tag{12}$$

where,

$$u_g = -\frac{1}{(1 + B\Delta f)} \frac{\partial h}{\partial y}, \qquad v_g = \frac{1}{(1 + B\Delta f)} \frac{\partial h}{\partial x}, \tag{13}$$

are the non-dimensional geostrophic velocity components. In retaining Rayleigh friction while neglecting nonlinearity, our most restrictive assumption is

$$R < E^{1/2}. \tag{14}$$

The source term on the right-hand side of (9) is zero over most of the basin, while the remaining terms are at least of order $R/S$. Substituting (11) and (12) into (9) then yields the shallow water planetary geostrophic equation with Rayleigh friction,

$$R \frac{\partial h}{\partial t} + \frac{\partial}{\partial x}(u_g \eta) + \frac{\partial}{\partial y}(v_g \eta) = E^{1/2} \left\{ \frac{\partial}{\partial x} \left( \frac{v_g \eta}{1 + B\Delta f} \right) - \frac{\partial}{\partial y} \left( \frac{u_g \eta}{1 + B\Delta f} \right) \right\}, \tag{15}$$

which is applicable away from the source and strong boundary currents. The right-hand side of (15) indicates that bottom friction acts like a diffusion operator on $h$.

Within a closed contour region, the geostrophic transport component is nondivergent and (15) becomes, to the leading order,

$$\frac{\partial}{\partial x}(u_g \eta) + \frac{\partial}{\partial y}(v_g \eta) = 0. \tag{16}$$

Flow evolution in this region depends crucially on the higher order effect of friction (Davey, 1978; Young, 1986). The first order balance is between upwelling and Rayleigh friction,

$$R \frac{\partial h}{\partial t} = E^{1/2} \left\{ \frac{\partial}{\partial x} \left( \frac{v_g \eta}{1 + B\Delta f} \right) - \frac{\partial}{\partial y} \left( \frac{u_g \eta}{1 + B\Delta f} \right) \right\}. \tag{17}$$

Assuming circular symmetry for the closed contour region for the sake of argument, and integrating (17) over an area enclosed by a closed geostrophic contour, we can

obtain an estimate of the velocity along a closed contour;

$$u = -\frac{R(1 + B\Delta f)r}{2E^{1/2}\eta}\int_0^r \frac{\partial h}{\partial t} r dr, \tag{18}$$

where $r$ is the distance of the contour from the center of the closed contour region (a stationary point in the geostrophic contour distribution). In dimensional form this becomes,

$$u = -\frac{f\tau r}{2(h + H - D)}\frac{\partial h}{\partial t}, \tag{19}$$

where we have assumed that the upwelling is independent of position within the closed contours. This is essentially the same results as that obtained by Kawase and Straub (1991) on an $f$-plane. Relation (19) now implies that a suitable velocity scale along closed contour is

$$U_c = \frac{f_c \tau Q L_0}{HL^2}. \tag{20}$$

where $f_c$ is the planetary vorticity at the center of the closed contour region. Using this velocity scale, the Rossby number takes the form $R_c$ given in Table 2.

In regions of blocked contours, frictional effects are usually only important in dissipative jets which form along lines of blocking. In combination with requirement (14), relations (10) and (15) imply that this will indeed be the case under the restrictions

$$SE^{1/2} < R < E^{1/2}. \tag{21}$$

Neglecting the dissipation terms in (15) yields,

$$R\frac{\partial h}{\partial t} + \frac{\partial}{\partial x}(u_g\eta) + \frac{\partial}{\partial y}(v_g\eta) = 0. \tag{22}$$

Using (13), we find that the transport divergence can be approximated by

$$\frac{\partial}{\partial y}(v_g\eta) = S\frac{\partial h}{\partial x}\left(\gamma\frac{\partial D}{\partial y} - B\frac{\partial \Delta f}{\partial y}\right). \tag{23}$$

If this is balanced by upwelling as in (22), then the meridional velocity is

$$v = \frac{\partial h}{\partial x} = \frac{R}{S}\frac{\partial h}{\partial t}\left(\gamma\frac{\partial D}{\partial y} - B\frac{\partial \Delta f}{\partial y}\right)^{-1}. \tag{24}$$

Continuity then suggests that the zonal velocity will scale as $u = \lambda^{-1}v$. Away from the northern and southern extremities of the basin, $\partial D/\partial y$ is small and the beta term in (24) will tend to dominate even when $\gamma > B$. In dimensional form, (24) then yields the Stommel and Arons (1960) velocity scale for interior blocked contour regions, $V_b = f_0 Q/\beta H L^2$. The corresponding along contour (zonal) velocity scale is

$$U_b = \frac{f_0 Q}{\beta H L L_0}. \tag{25}$$

Alternatively, if topography dominates, then the velocity scale would simply be $(B/\gamma)U_b$. A second Rossby number $R_b$, based on the blocked contour velocity scale (25), is defined in Table 2. It also follows from relations (20) and (25) that $U_b/U_c = L/(\beta\tau L_0^2)$, which is independent of the source strength and layer depth.

Rayleigh friction is associated with an ageostrophic flow component distributed over the entire layer depth. However, in a real fluid, most of the flow is geostrophic with dissipation concentrated in a bottom Ekman layer. In this case, the spin-down time for a fluid of kinematic viscosity $\nu$ is

$$\tau = \frac{H}{(\nu f_0/2)^{1/2}}, \tag{26}$$

(Gill 1982, p 354), while the corresponding Ekman pumping velocity (for zonal flow) is

$$w_E = \left(\frac{\nu}{2f_0}\right)^{1/2} \frac{\partial u}{\partial y} = \frac{H}{f_0 \tau} \frac{\partial u}{\partial y}, \tag{27}$$

(Gill, 1982, p 331). The velocity scale (20) for flow in closed contour regions, can be obtained directly from these results by assuming that the upwelling is balanced by Ekman pumping (i.e., $\partial h/\partial t = Q/L^2 = w_E$).

## 3. Numerical and laboratory models

Numerical solutions were obtained for the square basin geometry with sloping sidewalls and meridional ridge illustrated in Figure 1. The zonal width of the basin was 35 degrees and extended meridionally from 15N to 50N ($\approx$4000 km). Both the exponentially decaying side walls and the Gaussian ridge had horizontal $e$-folding scales of 3.5 degrees ($\approx$400 km). Eqs. (1)–(4) were solved using the enstrophy conserving scheme of Sadourny (1975) on a 100 by 100 Arakawa C-grid. This gave a resolution of 0.35 degrees ($\approx$40 km) which was always significantly less than the horizontal scale of the topography and the internal deformation radius. The scheme required that the layer depth always be greater than zero, restricting the experiments

in cases where all topographic features (including the sloping side walls) were totally submerged in the abyssal layer ($\gamma < 1$).

Each numerical run was initiated from a state of rest (with $u$, $v$ and $h$ equal to zero) by turning on the volume flux $Q$. The subsequent spin-up of the abyssal layer was recorded at 20 day intervals as new fluid entered the basin. Like the spin-up experiments of Kawase and Straub (1991), there was no sink for the new fluid, so that the depth anomaly $h$ increased steadily throughout the simulation.

The laboratory model consisted of a cubic plexiglass tank of dimension 70 cm (Fig. 1). Topography similar to that described for the numerical model was molded from plaster with a plywood frame. One side of the topography was slightly elevated to produce a slope of grade $\alpha$ which gives rise to a topographic beta effect of magnitude $\beta = \alpha f_0/H$.

For each experiment a deep layer ($H_* = 60$ cm) of fresh water was first brought to solid body rotation. A source of salty water, connected to a 2.0 cm diameter vertical pipe extending almost to the bottom, was then turned on. The source strength was sufficiently small and the reduced gravity sufficiently large (Table 1) that mixing with the upper layer was minor. Measurements began when the lower layer mean depth reached $H = 7$ cm. At this point a valid comparison could be made with the completely spun-up numerical solutions.

The laboratory model can be regarded as a reduced gravity shallow water system only if there is negligible flow in the upper layer. Chassignet and Cushman-Roisin (1991) used a scaling analysis of the equations of motion to derive conditions under which a deep layer would remain stationary for both small (deformation radius) and large (planetary scale) motions in the active layer. For our system the conditions can be written in the form

$$\frac{H_*}{H} + 1 \gg \max\left(1, \min\left(\frac{1}{S^2}, \frac{\gamma}{B}\right)\right). \tag{28}$$

This condition was marginally satisfied with the left-hand side 10 and the right-hand side 5, which was probably sufficient to ensure that upper layer flows were weak. During the course of the experiments, only a very weak surface circulation induced by stress from the overlying air could be detected.

Exact similarity of the numerical and laboratory models required matching of all the non-dimensional parameters listed in Table 2. However, approximate similarity can be achieved by matching only those that occur in the dynamic equations (7)–(9) along with $\lambda$ which appears in the boundary conditions. The aspect ratio, $\delta$, is difficult to replicate. It has been argued (e.g. Boyer and Chen, 1987) that provided that hydrostatics are maintained when $\delta$ is increased to 0(1), flow structures are stretched in the vertical but otherwise remain similar to the low aspect case. It can be easily

shown that vertical accelerations do not violate the hydrostatic balance if $\delta^2 R \ll 1$. In our configuration this condition is only violated right at the source.

Further restrictions which ensure relevance to ocean circulation are that the spin-down time must be far greater than a rotation period ($E \ll 1$); the deformation radius should be smaller than the horizontal topographic scale ($S \ll 1$) which in turn should be much less than the basin scale ($\lambda \ll 1$); and finally the most interesting case is one in which beta effects are not totally subsumed by topographic influences (say $0.1 < B < 1$). These, along with other experimental practicalities, restricted the study to a very small parameter space. However, this did not conflict with our principal aim of making direct comparisons with numerical simulations. We therefore chose to study laboratory flows under a single set of reasonably realistic conditions, varying only the source location.

## 4. Numerical results

The numerical spin-up process can be represented by the development of the interface perturbation. In geostrophic regions of the flow, isolines of this quantity follow streamlines. Figures 2 and 3 show the geostrophic contours at $t = 0$ and the development of the interface height for southwestern and northwestern sources respectively. The numerical conditions are those listed in Table 1. The pressure perturbation introduced at the source began by propagating around the outer perimeter of the basin at the Kelvin wave speed. The slower Rossby wave response could be identified after approximately 40 days. A planetary wave component spread the eastern boundary current westward, while a topographic component propagated northward along the western side of the ridge and southward along the eastern side. The combined effect was cyclonic flow along geostrophic contours.

The interface perturbation converged toward the closed contour region in the southern portion of each basin. However, since the Rossby waves followed geostrophic contours, they could not penetrate the closed regions. The layer depth therefore initially increased much more rapidly outside the closed region than within. This could not continue indefinitely, but had to be balanced by frictional effects (Kawase and Straub, 1991). Rayleigh friction allowed the depth anomaly to diffuse across geostrophic contours in accordance with Eq. (15). This supplied the required transport into the closed contour regions.

After approximately 100 days, the source location also became important. Provided dissipation was small, the source fluid retained a memory of its initial potential vorticity. If the source was at the same latitude as the closed contours, then energy could not propagate beyond this region except by frictional processes. After the Kelvin waves spun-down, most of the flow was restricted to the closed contours (as shown by the last contour plot in Fig. 2). Alternatively, if the source was located well to the north, cyclonic vorticity was generated and stored in the western and southern boundary currents. The effect of this was to form closed contours of potential

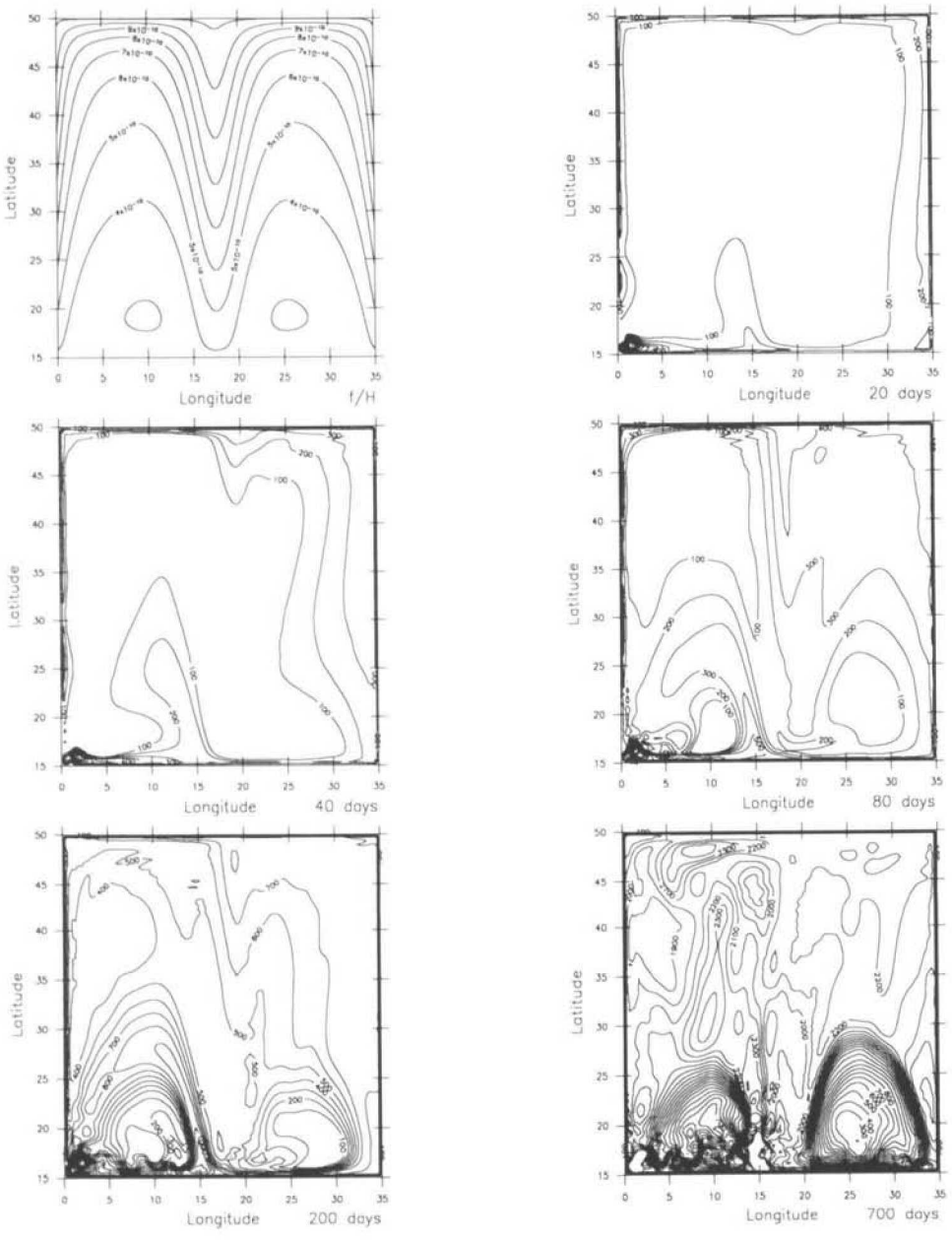


Figure 2. The geostrophic contour pattern (top left hand side, in (cm × sec.)$^{-1}$) and the development of the interface perturbation $h$ (in centimeters) during spin-up of a southwestern source flow. The conditions are listed in Table 1 (not underlined).

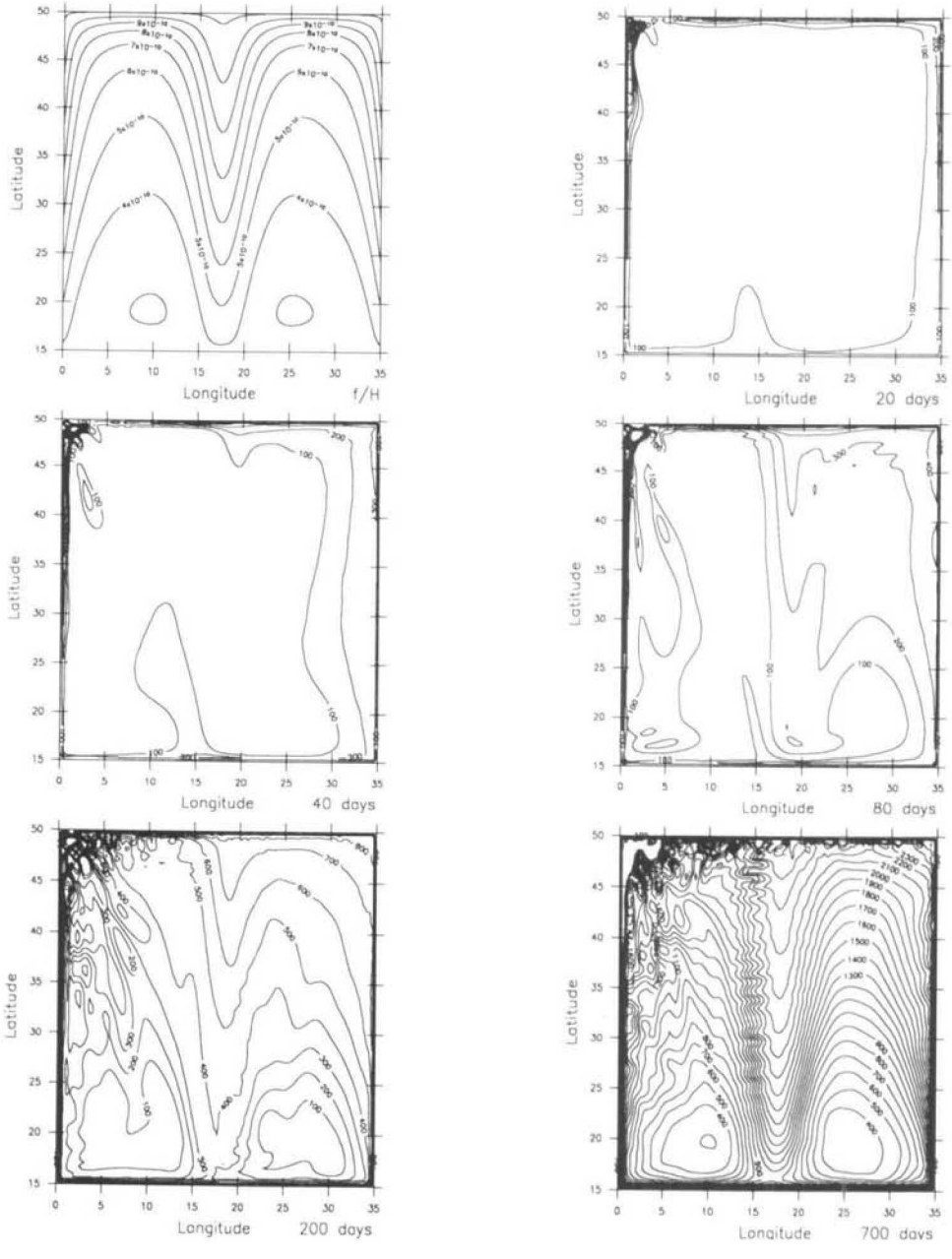


Figure 3. As in Figure 2, except that the source is in the northwest.

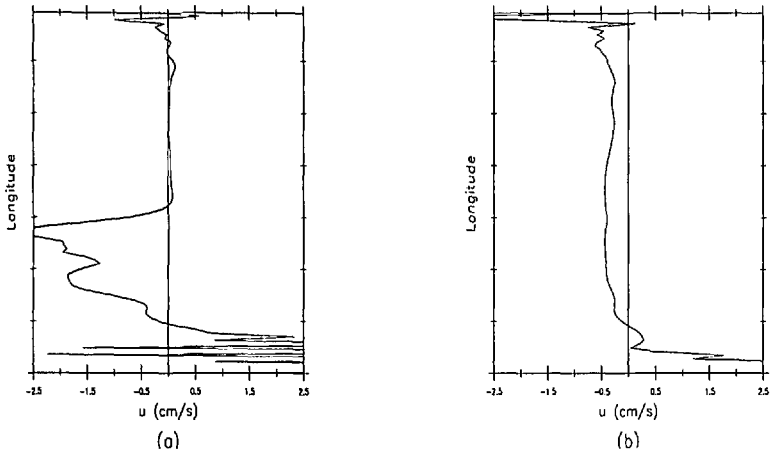


Figure 4. Meridional velocity sections at 26.25° taken from (a) the southwestern source flow in Figure 2 and (b) the northwestern source flow in Figure 3.

vorticity $(f + \zeta)/(h + H - D)$. This allowed the flow to return to northern latitudes along the eastern boundary, thereby filling most of the basin (last plot in Fig. 3). The dependence on source location tended to diminish as friction was increased. In more viscous flows (not shown), cyclonic vorticity stored in the boundary current was dissipated before it could return to the north, leaving most of the flow trapped at lower latitudes.

Considerable amounts of eddies are generated in the region of the source due to local instability of the flow. Influence of these eddies, however, is mainly confined to the boundary region adjacent to the source. The last panel of Figure 3 shows short wavelength perturbations along the western flank of the mid-ocean ridge. They make up a packet of transient short Rossby waves with a pseudoeastward group velocity which was generated when the long wave signal reached the western boundary and was reflected.

A series of simulations were run in order to test the scalings presented in Section 2. A meridional transect of the zonal velocity bisecting the eastern closed contour region (longitude 26.25°) was used for the comparison. Examples of transects for both southwestern and northwestern sources are presented in Figure 4. The meridional gradient of the zonal velocity, non-dimensionalized in accordance with relation (20), is plotted as a function of spin-down time in Figure 5. The scaling is consistent with the numerical output for spin-down times of order 100 days or less. However, the velocity gradients for a northwestern source are typically half those for a southwestern source. For longer spin-down times $R_c$ exceeds $E^{1/2}$, which violates condition (14). Non-linearity is then important and the scaling is no longer applicable. Figure 5 indicates that the non-dimensional velocity then decreases as the dissipative effects of eddies become significant.

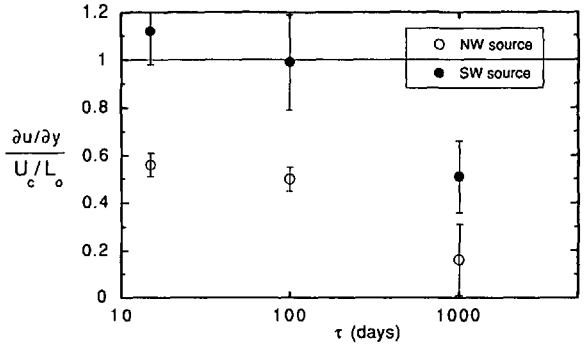


Figure 5. The meridional velocity shear within closed geostrophic contours, non-dimensionalized in accordance with relation (20), plotted as a function of spin-down time for northwestern and southwestern sources. The error bars represent the range of slopes which might reasonably be fitted to each velocity section.

The velocity along the contour outside the closed contours (longitude 26.25°), non-dimensionalized in accordance with relation (25), is plotted against the spin-down time in Figure 6. For a southwestern source, this velocity is always small, consistent with the notion that waves cannot penetrate past the closed contour region. However, the scaling does appear to be applicable to the northwestern source for spin-down times of 100 days or more. For shorter spin-down times, friction becomes important with $R_c > SE^{1/2}$, violating condition (21). Under these circumstances, the flow characteristics are almost independent of the source location. In contrast to closed contour regions, nonlinearity remains a second-order effect in blocked regions. This is because $R_b < E^{1/2}$ even for relatively long spin-down times.

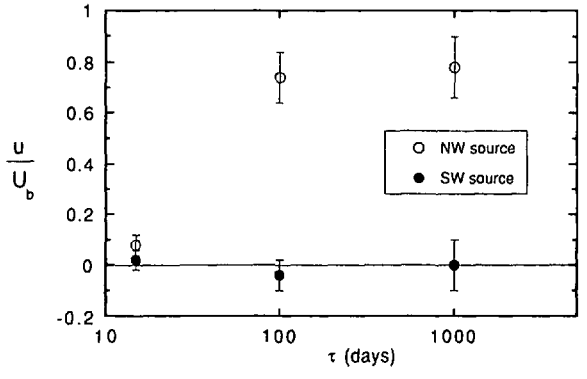


Figure 6. The meridional velocity along blocked geostrophic contours, non-dimensionalized in accordance with relation (25), plotted as a function of spin-down time for northwestern and southwestern sources. The error bars represent variations in velocity along each section.

## 5. Laboratory results

The laboratory experiments were visualized by adding dye to the source fluid after the lower layer depth had reached its prescribed level ($H = 7$ cm). The spread of the dye cloud was recorded using still photographs and time-lapse video. Figure 7 shows the flow for both southwestern (left photographs) and northwestern (right photographs) sources. This should be interpreted in terms of the laboratory geostrophic contour pattern shown in Figure 8. Centrifugal accelerations, which cause the layer interface to take the form a paraboloid, were taken into account in calculating the laboratory geostrophic contours. The laboratory and numerical models share the essential elements of the pattern of the geostrophic contours such as the two closed contour regions separated by the mid-ocean ridge. Differences between the two are attributable to the spherical geometry of the earth in the numerical model. Figure 7 should also be compared with the numerical solution in Figure 9, for which the similarity conditions discussed in Section 2 were satisfied.

The general features of the laboratory flow were comparable to the numerical solutions obtained using similar conditions. For example, flow from the southwestern source was tightly confined within the closed contour regions and flow between these regions was considerably restricted by the ridge. In contrast, most of the northwestern source fluid followed the outer perimeter of the tank, negotiated the ridge, and finally separated from the eastern boundary. The western boundary portion of this flow was unstable, resulting in spurts and filaments that invaded the interior as seen in the top right panel of Figure 7. These appear to be due to local flow instabilities rather than instabilities in the source region found in the numerical model. The resulting northward penetration of the recirculating flow was clearly greater than the southwestern source case, although the eastern boundary current appeared weaker than would be suggested by Figure 9. Velocity sections were also recorded from dye lines, produced at wire electrodes in a bromothymol blue solution added to the active layer (Baker, 1966). These suggested a general structure similar to that in Figure 4. While the unsteady nature of the flow made quantitative comparisons difficult, velocity magnitudes appeared to be consistent with relations (20) and (25).

There were also some significant differences in the details of the numerical and laboratory flows. The most notable was more large amplitude waves and eddies in the interior region of the laboratory model. These appeared to contribute significantly to the cross contour transport in the experiments, thereby supplementing the Ekman transport. This was particularly evident for the southwestern source near the border between the closed and blocked contours. Indeed, the experiments suggest that this border region, which is characterized by high shear, is an important site for eddy generation in the basin interior.

Waves periodically formed near the eastern boundary, then propagated along geostrophic contours in a pseudo-westward direction (Fig. 10). Most of the energy

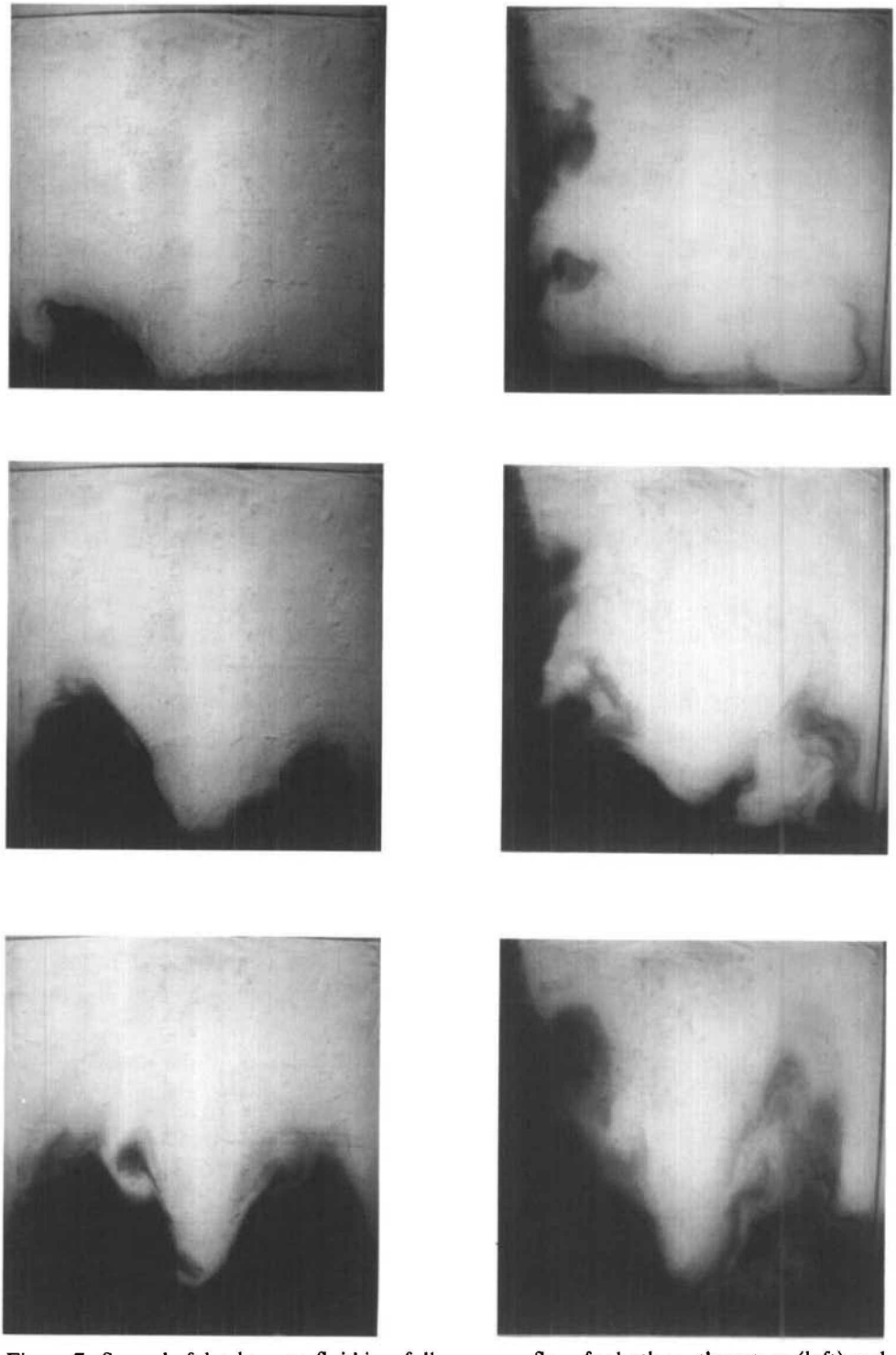

Figure 7. Spread of dyed source fluid in a fully spun-up flow, for both southwestern (left) and northwestern (right) sources. The top photographs correspond to 143 rotations, the center to 430 rotations and the bottom to 783 rotations after the source was dyed. The conditions of the experiment are listed in Table 1.

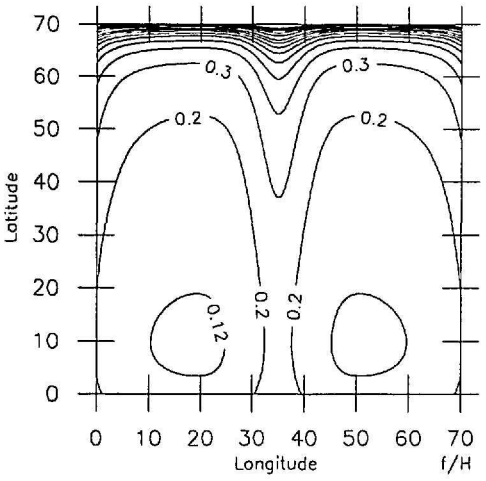


Figure 8. The geostrophic contour pattern calculated for the laboratory experiments. Distortion of the interface height due to centrifugal acceleration has been taken into account.

travelled at measured wavespeeds of $c = -0.32 \pm 0.05$ cm s$^{-1}$, which is at least an order of magnitude higher than the mean flow. A linear planetary wave interpretation, suggests that the wavelength of these features should be $2\pi(c/\beta)^{1/2} = 21 \pm 3$ cm. Such a length scale could have been determined by the characteristic zonal length scale of the individual basins. Alternatively, it may have been set by baroclinic

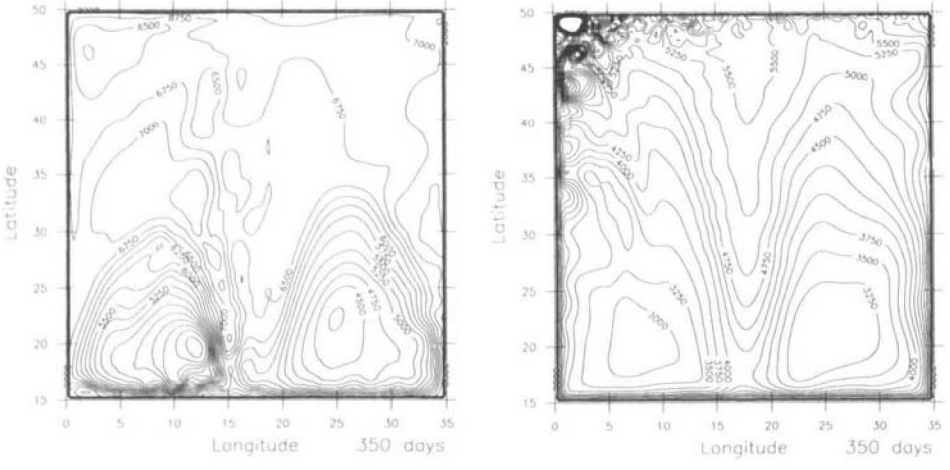


Figure 9. The inteface perturbation $h$ after 350 days for southwestern (left) and northwestern (right) sources. The conditions are listed in Table 1 (underlined). Note that the flow patterns are very similar to those in Figures 2 and 3. Although friction is stronger in the present case, so is the magnitude of the mass source, resulting in flow speeds and Rossby number that are similar to the previous case.

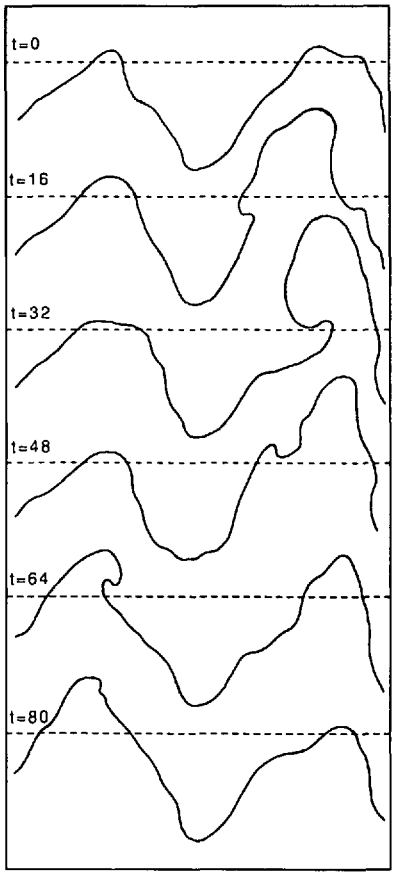


Figure 10. A time series for the shape of the northern edge of the dye cloud for the southwestern source (taken from video records). The time is in units of rotation periods and the dashed line represents the mid-latitude of the basin $\theta_0$. At $t = 0$ there is little evidence of large amplitude waves and the edge of the dye cloud corresponds roughly to the outer edge of the closed contour region. As time progresses, a wave grows in the eastern basin ($t = 16$), breaks ($t = 32$) and propagates westward along geostrophic contours. By $t = 80$ the energy has propagated southward along the western boundary of the basin.

instability of the mean flow, for which the fastest growing linear mode has wavelength $2\pi(g'H)^{1/2}/f = 24$ cm.

Successive waves were often observed to grow in amplitude until a deformation radius scale eddy formed in the eastern basin (Fig. 10). This feature was subsequently destroyed as it interacted with the ridge, presumably resulting in significant dissipation. However, some of the energy continued westward in the form of a less coherent wavetrain, then propagated southward along the western boundary. The periodicity was about one event every 70 rotations. This corresponds to the approximate time for a wave to propagate at the speed $c$ around a closed loop encircling the

two closed contour regions. From this perspective, these particular wave motions may be viewed as a resonant phenomena.

## 6. Conclusion

The models confirm the dominant role of Rossby waves in setting up the circulation and the importance of closed geostrophic contours in the development of strong abyssal flow regions. Perhaps less expected was the strong influence of the source location, whose latitude determined the meridional penetration of the abyssal gyre. The model results imply that ocean basins with deep water sources in their own hemisphere (e.g. North Atlantic and South Pacific basins) will contain abyssal gyres which can cross geostrophic contours and fill the basin. On the other hand, gyres in basins with sources in the opposite hemisphere (e.g. South Atlantic and North Pacific basins) will tend to be restricted to a closed contour region which can usually be found at the equatorial end of the basin.

A frictional balance in closed contour regions allows inflow from blocked contour regions. This has been confirmed in simulations with Rayleigh friction in which an ageostrophic flow component carries the cross-contour flux as suggested by Kawase and Straub (1991). In a real fluid, the transport may be concentrated in the bottom Ekman layer. However, the laboratory experiments suggest that eddy fluxes can also be important. For a southwestern source, the border between closed and blocked contours is characterized by high shear and is an important site for the generation of eddies in the basin interior.

Perhaps the major limitation of the models was their low vertical resolution. This is particularly restrictive from the veiwpoint that density interfaces never intersect the topography. This excludes hyposometric effects which add a divergent component to the flow and thus the possibility of anticyclonic circulation. While these effects can be easily included in a continuously stratified laboratory experiment, the planetary vorticity gradient would no longer be meaningfully represented by sloping topography. More sophisticated numerical models (such as the isopycnic coordinate model of Bleck and Boudra, 1986) are computationally intensive, but include multiple layers which can intersect topography.

*Acknowledgments.* We thank Peter B. Rhines for his guidance, encouragement and the laboratory facility. SAC would like to acknowledge the support of the University Corporation for the Atmospheric Research through a postdoctoral fellowship in ocean modeling. MK would like to acknowledge the support of ONR grant N00014-90-J-1102 and NSF grant OCE 9104859.

## REFERENCES

Baker, D. J. 1966. A technique for the precise measurement of small fluid velocities. J. Fluid Mech., *26,* 573–575.

Bleck, R. and D. Boudra. 1986. Wind-driven spin-up in eddy-resolving ocean models formulated in isobaric coordinates. J. Geophys. Res., *91,* 7611–7621.

Blumen, W. and B. D. Gross. 1987. Semigeostrophic flow over orography in a stratified rotating atmosphere. Part 1: Steady three-dimensional solutions over finite ridges. J. Atmos. Sci., *44,* 3007–3019.

Boyer, D. L. and R. Chen. 1987. Laboratory simulation of mountain effects on large-scale atmospheric motion systems: The Rocky Mountains. J. Amost. Sci., *44,* 100–123.

Boyle, E. A. and L. Keigwin. 1987. North Atlantic thermohaline circulation during the past 20,000 years linked to high-latitude surface temperature. Nature, *330,* 35–40.

Cessi, P. and J. Pedlosky. 1986. On the role of topography in the ocean circulation. J. Mar. Res., *44,* 445–471.

Chassignet, E. P. and B. Cushman-Roisin. 1991. On the influence of a lower layer on the propagation of nonlinear ocean eddies. J. Phys. Oceanogr., *21,* 939–957.

Davey, M. K. 1978. Recycling flow over bottom topography in a rotation annulus. J. Fluid Mech., *87,* 497–520.

de Szoeke, R. A. 1985. Wind-driven mid-ocean baroclinic gyres over topography; extension of the Sverdrup relation. J. Mar. Res., *44,* 793–824.

Gill, A. 1982. Atmosphere-Ocean Dynamics. Academic Press, New York, 662 pp.

Hautala, S. L. and S. C. Riser. 1989. A simple model of abyssal circulation, including effects of wind, buoyancy and topography. J. Phys. Oceanogr., *19,* 596–611.

Hogg, N. G. 1989. Finite amplitude effects on deep planetary circulation over topography. J. Phys. Oceanogr., *19,* 1697–1706.

Haung, R. X. 1990. On the three-dimensional structure of the wind-driven circulation of the North Atlantic. Dyn. Atmos. Oceans, *15,* 117–159.

Johnson, E. R. 1983. Taylor columns in a horizontally sheared flow. Geophys. Astrophys. Fluid Dyn., *12,* 35–43.

Kawase, M. and D. Straub. 1991. Spin-up of a source driven circulation in an abyssal basin in the presence of bottom topography. J. Phys. Oceanogr., *21,* 1501–1514.

Labeyrie, L. D., J. C. Duplessy and P. L. Blanc. 1987. Variations in mode of formation and temperature of oceanic deep waters over the past 125,000 years. Nature, *317,* 477–482.

McCartney, M. S. 1975. Inertial Taylor columns on a beta plane. J. Fluid Mech., *68,* 71–95.

Rhines, P. B. 1989. Deep planetary circulation and topography. Simple models of midocean flows. J. Phys. Oceanogr., *19,* 1449–1470.

Sadourny, R. 1975. Compressible model flows on the sphere. J. Atmos. Sci., *32,* 2103–2110.

Smith, R. B. 1979. The influence of mountains on the atmosphere. Ad. Geophys., *21,* 87–230.

Stommel, H. and A. B. Arons. 1960. On the abyssal circulation of the world ocean—I. Stationary planetary flow patterns on a sphere. Deep Sea Res., *6,* 140–154.

Straub, D. N. and P. B. Rhines. 1990. Effects of large-scale topography on abyssal circulation. J. Mar. Res., *48,* 223–253.

Thompson, L. 1990. Flow over finite topography. Ph.D. thesis, MIT-WHOI Joint Program in Oceanography and Oceanographic Engineering, 222 pp.

Welander, P. 1969. Effects of planetary topography on the deep-sea circulation. Deep-Sea Res. *16* (Suppl), 369–391.

Young, W. R. 1986. Baroclinic theories of wind driven circulation, *in* General Circulation of the Ocean, H.D.I. Abarbanel and W. R. Young, eds., Springer, New York, 134–201.

Received: *17 December, 1991;* revised; *14 July, 1992.*